Taylor & Francis
Taylor & Francis Group

RESEARCH ARTICLE

Black phosphorus conjugation of chemotherapeutic ginsenoside Rg3: enhancing targeted multimodal nanotheranostics against lung cancer metastasis

Jie Xiong[a], Hongmei Yuan[b], Hongge Wu[a], Jing Cheng[a], Shengli Yang[a] and Ting Hu[a]

[a]Cancer Center, Union Hospital, Tongji Medical College, Huazhong University of Science and Technology, Wuhan, China; [b]Department of Pathology, Wuhan Jinyintan Hospital, Wuhan, China

ABSTRACT

It is a significant challenge in lung cancer chemophotothermal (CPT) therapy to develop multifunctional theranostic nanoagent (MTN) for precise targeting and successful tumor treatments, especially for lung metastasis. To overcome this problem, we effectively design and construct multifunctional black phosphorus (BP) nanoagents, BPs/G-Rg3@PLGA. BPs quantum dots (BPsQDs) are co-loaded onto poly(lactic-co-glycolic acid) (PLGA) with subsequent conjugations of a cancer therapeutic compound, ginsenoside Rg3 (G-Rg3), in this composite nanoagent. The *in vivo* delivery findings suggest that BPs/G-Rg3@PLGA has an excellent affinity for primary tumors and metastatic lung tumors. Furthermore, when paired with near-light irradiation, BPs/G-Rg3@PLGA shows superior controllable CPT therapy synergetic therapeutics, significantly increasing photothermal tumor ablation effectiveness. Mechanistically, heating causes rapid G-Rg3 release from the non-complex, and thermal therapy induces apoptosis, culminating in the reduction of lung cancer metastasis. Additionally, *in vivo* and *in vitro* findings support the biocompatibility of BPs/G-Rg3@PLGA. This thesis identifies a versatile BPs-based MTN for lung cancer metastasis control.

1. Introduction

Cancer remains a significant cause of death and a major global health problem. Breast cancer is a prevalent form of cancer and is an actual cause of female cancer death (Oku et al., 1997; Wang et al., 2010; Lin et al., 2016; Xu et al., 2016; Wan & Ping, 2021). Although primary tumors cause immense morbidity, most people have a recommended forecast after prior tumor removal, even without chemotherapy. Once, however, tumor cells metastasize to restricted organs, including the lungs, bones, and brains. The diagnosis is incurable without available specific medicinal products, with metastatic conditions that account for over 90% of the mortality from breast cancer (Low & Kularatne, 2009; Liang et al., 2016; Gao et al., 2019). Little is clear, though, on the way to metastatic therapy even though ongoing efforts in various fields of nanomedicine have been invested (Song et al., 2016).

Most efforts are focused on nanomedicine for cancer in developing therapeutic techniques to enhance physical–chemical properties, such as the parameters of 3 S (size, structure, and surface) and electrostatic interactions (Nguyen et al., 2019; Qian et al., 2019; Xu et al., 2020). However, nanocomposites' properties have rarely been evaluated as tumor killers or as site-accurate vehicles for tumor control. Recently, black phosphorus (BP) has higher physicochemical properties than other double-dimensional nanocomposites as an emerging star of materials research and has strong promise

in a broad range of cancer therapies and diagnoses (Sung et al., 2011; Suetsugu et al., 2013; Sang et al., 2019). In particular, in cancer therapies, BPs have been tested with medicinal and gene administering and photochemotherapy. Previous findings have shown that its excellent drug-loading and delivery abilities have encouraged the cancer-tutoring effectiveness of BP (Ou et al., 2018; Geng et al., 2019; Li et al., 2019). Meanwhile, as described in a recent paper, they have found the unique chemical toxicity of BPs to cancerous cells. However, tremendous obstacles still have to be confronted. In conjunction with the symptoms of tumors, BP-based nanocomposites, versatile chemthermal therapies, and unique treatments for advanced tumors have to be established (especially lung metastasis) (Raucci et al., 2019).

Phosphorus is a crucial element for human beings and is indispensable in cellular and biological components and biodegradability applications that endow BPs with superior biocompatibility and successful interactions with nano-bio and biomedical biodegradability (Li et al., 2017; Chen et al., 2018; Wang et al., 2019). The rationale for BP's tumor location-sensitive investigations as platforms for drug distribution and therapeutic agents are raised by such distinctive features. An multifunctional theranostic nanoagent (MTN)-BPs based nanodrugs for precise nanomedicines against the metastasis in lung cancer has been developed in this study to control the metastasis of breast cancer. Our combined results

CONTACT Shengli Yang ✉ Shengli-Yang@hotmail.com; Ting Hu ✉ tinghu618@yahoo.com 📍 No. 1277, Jiefang Avenue, Wuhan 430022, China
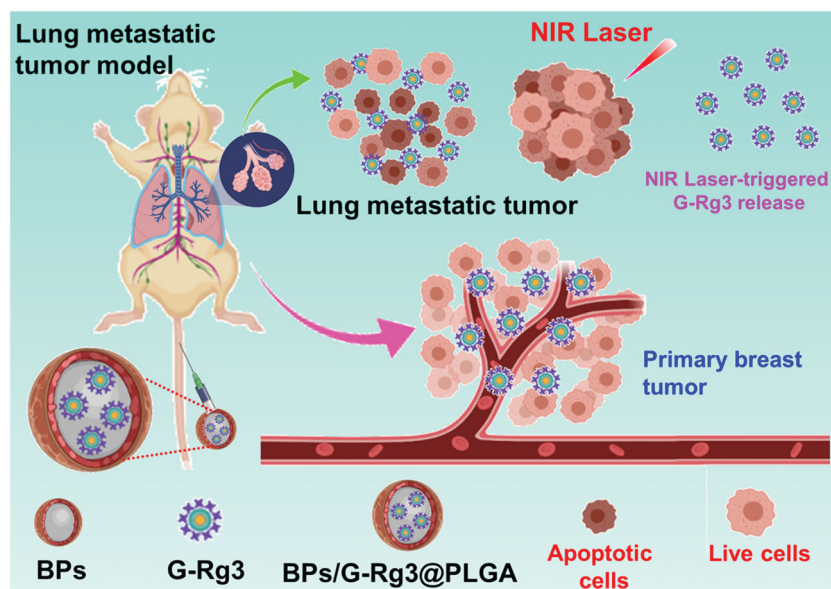
Figure 1. Schematic representation of enhanced new multifunctional nanocomposite, focused on BPs, to suppress metastasis of breast cancer by BPs/G-Rg3@PLGA.

uncovered a new multifunctional nanocomposite focused on BPs to suppress breast cancer metastasis (Figure 1).

2. Experimental

2.1. Fabrication of BPsQDs

BPs crystals were purchased from Smart-Elements (Vienna, Austria). 1-Methyl-2-pyrrolidinone (NMP, 99.5%, anhydrous,) was obtained from the Sigma-Aldrich Co., LLC (Santa Barbara, CA). All the chemicals used in this study were at the analytical reagent grades. BPsQDs were synthesized with the liquid exfoliation method, as reported in recent report (McAllaster & Cohen, 2011; Yun et al., 2017; Tian et al., 2021). In briefly, 20 mg of BPs powders were dispersed in 20 mL NMP, and the mixture was thereafter sonicated with a sonic tip at an ultrasonic frequency of 19–25 kHz for 4 h with 2 s duration plus the interval of 4 s at a power of 1200 W. Afterwards, the mixture was further sonicated overnight in an ice bath at a power of 300 W. Finally, BPQDs dispersed in supernatant were collected after centrifugations at 7000 rpm for 20 min. Prior to nanocomposite synthesis, the obtained BPQD supernatants were further centrifuged at 12,000 rpm for 20 min, and then washed three times with dichloromethane (DCM) in order to get high-quality BPsQDs.

2.2. Preparation of BP/Cy5.5@PLGA and BPs/G-Rg3@PLGA

Polyvinyl alcohol (PVA, MW: 9000–10,000), PLGA (50:50, MW: 40,000–70,000) and DCM solutions were acquired from the Sigma-Aldrich (Shanghai, China). Cy5.5 NIR fluorescence dye was obtained from the Innova Biosciences (Cambridge, UK). The above prepared BPQDs were redisposed in PLGA DCM solution (10 mg/mL, 1 mL) containing 2 mg Cy5.5. Further, G-Rg3 was similarly loaded onto the materials (Mu et al., 2017;

Zhao et al., 2019; Wu et al., 2021). After sonication for 5 min by ultrasonic homogenizer (SCIENTZ-1200E, Ningbo, China), the mixtures were re-suspended in 0.5% (w/v) PVA aqueous solutions (10 mL) and afterwards sonicated for 5 min. The emulsions were further stirred overtime at the RT to remove the residual solutions of DCM. Final materials were obtained by centrifuging at 7000 rpm for 15 min and washed twice with deionized (DI) water.

2.3. Morphology and characterization of nanocomposites

BPs concentrations were determined by inductively coupled plasma atomic emission spectroscopy (Agilent 8800, Tokyo, Japan), as described in our studies. SEM imaging was performed on a field-emission SEM (NOVA NANOSEM430, FEI, Eindhoven, Netherlands) at 5–10 kV after gold coating for 120 s (EM-SCD500, Leica, Wetzlar, Germany). TEM imaging was assessed using a high resolution JEOL JEM 2010 F TEM (Hitachi Scientific Instruments, Tokyo, Japan). The ultraviolet–visible–near infrared (UV–vis–NIR) absorption spectra were obtained on a UV–vis–NIR spectrometer with integrating sphere attachment (ISR-2600 Plus; Shimadzu UV-2600, Kyoto, Japan). The FTIR spectra were recorded with a Thermo-Nicolet Nexus 6700 FTIR spectrometer (Madison, WI).

2.4. Drug loading content (LC), encapsulation efficiency (EE), and release determination

G-Rg3 content was examined by high-performance liquid chromatography (HPLC), as reported (Ou et al., 2018). To measure LC and EE for G-Rg3 on the nano platform, 0.5 mg BPs/G-Rg3@PLGA nanospheres (NSs) was dissolved in 0.5 mL DCM, and DCM was then removed by vacuum drying oven (DZF-6020, Yiheng Ltd, Jinan, China). The residue was

re-dissolved in acetonitrile–water (50:50 v/v) solution (1 mL) and stored in a vial for HPLC measurement. The samples were injected into a reverse-phase C-18 column and eluted with a mobile phase consisting of acetonitrile–water (50:50 v/v) at a flow rate of 1.0 mL/min. G-RG3 concentration was analyzed using a UV detector (227 nm). The following equations, respectively calculated LC and EE:

$$LC\ (\%) = \frac{\text{weights of the G–Rg3 in NSs}}{\text{weights of the NSs}} \times 100\%$$

$$EE\ (\%) = \frac{\text{weights of the G–Rg3 in NSs}}{\text{weights of the feeding G–Rg3}} \times 100\%$$

To characterize G-Rg3 release, BPs/G-Rg3@PLGA (5 mg) were dispersed in phosphate buffer solution (PBS, 1 mL) at pH 6.5 containing 0.1% w/v Tween 80. The suspended materials were added into a dialysis bag (MWCO = 3500), followed by dialysis in PBS (20 mL) with slow stirring at 200 rpm at 37 °C. At different time points, the outside PBS was replaced with fresh PBS and was subjected to G-Rg3 detection by HPLC. The suspended materials were radiated by NIR laser at 808 nm (1.0 W/cm^2) for 5 min before dialysis for the group upon NIR radiation.

2.5. Photothermal performance assessment

The photothermal effect of BPs/G-Rg3@PLGA was assessed under 808 nm-continuous wave laser (GCSLS-05-007, Daheng New Epoch Technology, Inc., Beijing, China) at different concentrations for 600 s at a density power of 1.0 W/cm^2. The temperature change was recorded by an infrared camera thermographic system (FLIR SC 620, FLIR System, Inc., Wilsonville, OR) and thermocouple (TES 1315, TES Electrical Electronic Corp., China) (Shi et al., 2013; Song et al., 2015; Wang et al., 2020).

2.6. Cell culture and animal models

Our laboratory established the sub-line 4T1-luc derived from murine 4T1 breast carcinoma cell lines (4T1-luc cells) in our laboratory with standard culture conditions. The Animal Ethics Committee of the Research Center (approved no. 2019; file no. 4587TH) for Cancer Center, Union Hospital, Tongji Medical College, Huazhong University of Science and Technology, Wuhan, China. BALB/c female mice (7–8 weeks old) were purchased from the Vital River Laboratory Animal Technology Co. Ltd. (Beijing, China). According to previous reports, the 4T1 breast carcinoma lung metastasis model including the orthotopic models and intra tail-vein injections models were set up (Cheng et al., 2019; Boix-Montesinos et al., 2021; Jiang et al., 2021). In the orthotopic model experiments, when the primary tumor volume reached 100 mm^3, mice with comparable tumor volume were selected and randomly separated into various groups for ensuing the treatments. Tumor volume was examined by calipers and considered affording to the following equations: tumor volume=(length × width^2)/2. Since our cells were labeled with exotic luciferase genes, metastasis was monitored by bioluminescent imaging in each mouse after intraperitoneal

(i.p.) injections of 100 μL D-Luc (15 mg/mL, XenoLight, PerkinElmer, Waltham, MA) on an IVIS Spectrum Imaging System (Caliper Life Sciences, Hopkinton, MA). The photon flux was quantified and analyzed using the total flux with the Spectrum Living Image 4.0 software on an IVIS Spectrum Imaging System (Caliper Life Sciences Inc., Hopkinton, MA). After mice were sacrificed, primary tumors, organs and lungs were dissected and fixed in 4% PBS-buffered paraformaldehyde, followed by hematoxylin and eosin (H&E) staining concerning the standard instructions. Tissue sections were examined by an optical microscope (Axio Scope A1, Carl Zeiss, Inc., Jena, Germany).

2.7. Assessments of *in vitro proliferation and cellular uptake*

Ater various treatments, cells were washed thrice with PBS solutions, and then cell proliferation was determined by Cell Counting Kit-8 (CCK-8) assay following the instructions from the manufacturer (Solarbio, 1000T, Beijing, China). For the co-staining of calcein-AM and propidium iodide (PI), 4T1 cells were first exposed to BPs/G-Rg3@PLGA for 6 h with or without NIR radiation, followed by co-staining with calcein AM and PI. Green color denotes calcein AM staining and red color indicates PI staining, respectively. To determine the cellular uptake of nanocomposites, cells were washed and collected after treatment with Cy5.5-labeled BPs@PLGA at 50 μg/mL for 4 h, followed by fixing in 4% paraformaldehyde for 15 min. Afterwards, cellular nuclei were counterstained with DAPI for 20 min and washed three times with PBS. Finally, fluorescent imaging was recorded on a confocal laser scanning microscope (CLSM) (Mohamed Subarkhan et al., 2016, 2018; Subarkhan & Ramesh, 2016; Balaji et al., 2020; Sathiya Kamatchi et al., 2020).

2.8. Tissue distribution of nanocomposites in animals

4T1-Luc-derived mice bearing orthotopic tumors were intravenously (i.v.) inoculated with Cy5.5-labeled BPs@PLGA through the tail vein. Primary tumors and various organs were collected and subjected to bio-luminescent and fluorescent imaging on an IVIS System Spectrum Imaging (Caliper Life Sciences Inc., Hopkinton, MA) at different time points (n = 3 at each point). The photon flux was quantified and analyzed using the total flux with the Spectrum Living Image 4.0 software on an IVIS System Spectrum Imaging.

2.9. Statistical analysis

All of the data are represented as the means ± SD. The statistical significance between the measurements was evaluated using Student's *t*-test. A *p* value less than .05 was deliberated statistically significant, whereas a *p* value less than .01 was deliberated highly significant.
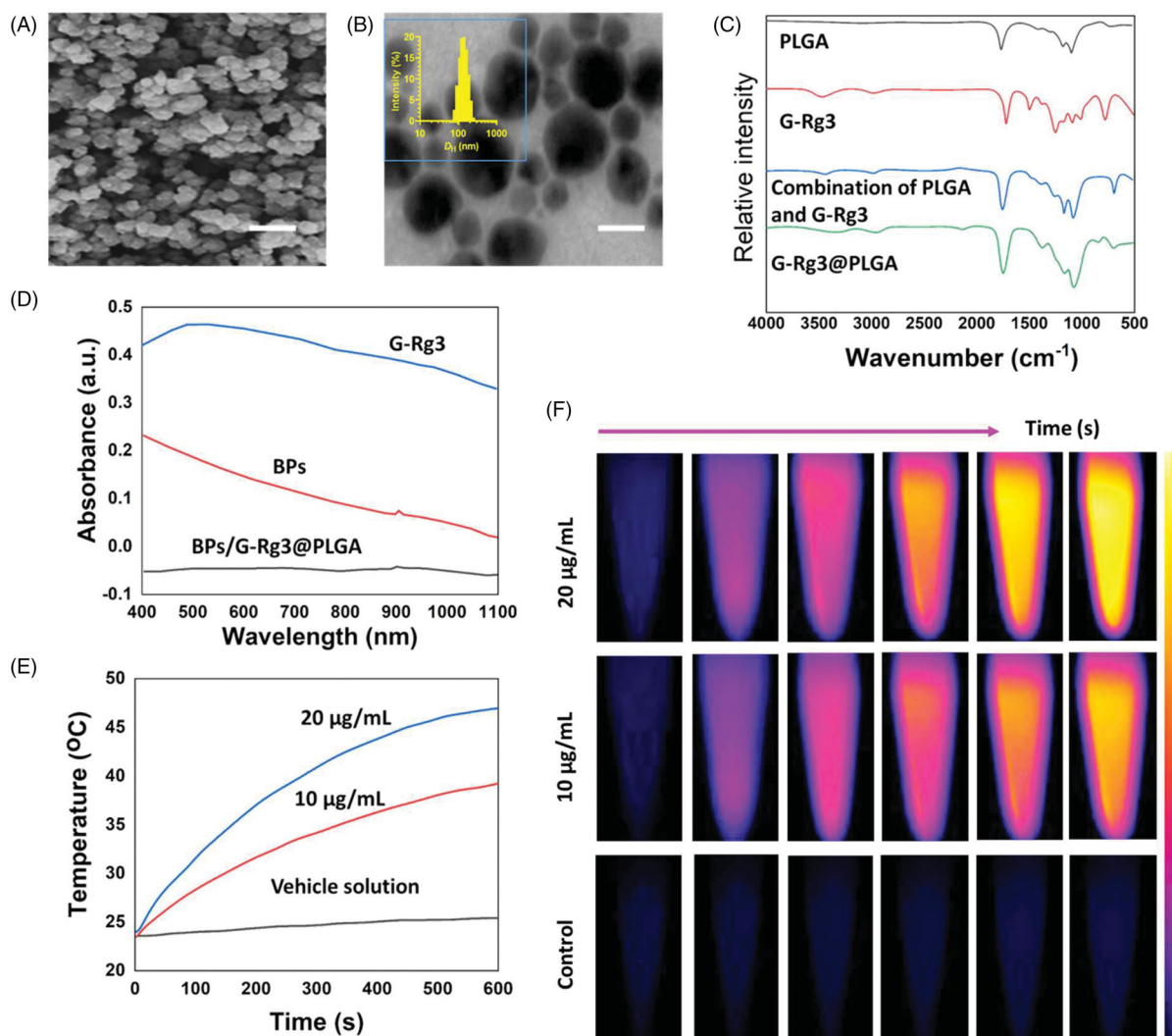
Figure 2. Fabrication and characterizations of BPs@PLGA. (A) SEM investigation of BPs@PLGA. Scale bar 100 nm. (B) TEM examination of BPs@PLGA (inset: size distribution of BPs@PLGA). Scale bar 200 nm. (C) FT-IR spectral analysis of PLGA, G-Rg3, combination of PLGA and G-Rg3, and G-Rg3@PLGA nanocomposites. (D) UV–vis–NIR absorptions spectral analysis of BPs/G-Rg3@PLGA, BPs, and G-Rg3. (E) Temperature elevations of BPs/G-Rg3@PLGA at various concentration under laser 808 nm NIR radiations at a densities for 600 s of 1.0 W/cm². (F) IR-thermal imaging of BPs/G-Rg3@PLGA at various concentration (s).

3. Results and discussion

3.1. Synthesis and characterizations of BPs@PLGA

BPs quantum dots (BPsQDs) have been incorporated in poly(-lactic-co-glycolic acid) (PLGA), delivering BPs@PLGA, in order to increase drug load capability and tumor targeting (Deng et al., 2017; Mayorga-Martinez et al., 2018; Hu et al., 2020; Biedulska et al., 2021). PLGA is a form of bio-degradable and bio-compatible polymer approved by the Food and Drug Administration (FDA), which is commonly used for the delivery of nanodrugs and therapeutic agents. A solution with a monodispersity of ∼130 nm (the desired size to focus on the tumor, via the improved permeability and retention (EPR) mechanism as described in the scanning electron microscopy (SEM) and transmission electron microscopy (TEM), the achieved BPs@PLGA shows a unified spherical morphology (Figure 2(A,B)). Then, ginsenoside Rg3 (G-Rg3), a major chemotherapeutic agent for breast cancer, was loaded into BPs@PLGA. Fourier transform infrared (FT-IR), distinguished by characteristic peaks of the ether bonds (situated about

1731 cm⁻¹) for G-Rg3 and the extended vibration peaks for PLGA, are verified as presented in Figure 2(C). Figure 2(C) demonstrates the active encapsulations of G-Rg3. Attributable to the relationship among the carboxyl acid in the ester group and PLGA in G-Rg3, the absorption peak indicates of G-Rg3 were overest in BPs/G-Rg3@PLGA (Figure 2(C)). In addition, 12% and 92%, respectively, have been estimated for the drug LCs and EE of G-Rg3 and BPs@PLGA.

3.2. Chemothermal features of BPs/G-Rg3@PLGA

We address the structural features of BPs/G-Rg3@PLGA in the following section. The noticeable illustrative absorption spectral profiles from inside NIR regions due to the innately absorbable features of BPQDs were sufficiently preserved in BPs/G-Rg3@PLGA (Figure 2(D)), which offers the premise of the photothermal regime compared with the G-Rg3 UV–vis–NIR absorption spectra. The photothermal effect was investigated under laser radiation of 808 nm NIR. A quick

indentations temperature of ∼25 °C in BPs/G-Rg3@PLGA was exhibited, as shown in Figure 2(E), on 20 μg/mL following 600 s NIR radiations and a very fast temperature increase in the solution at 10 μg/mL was also observed. In comparison, the vehicle solution showed an insignificant temperature fluctuation (Figure 2(E)). To support these findings, BP/G-Rg3@PLGA's photothermal efficiency was further supported by the thermal infrared imaging investigation (Figure 2(F)). These data show that PLGA integrations and G-Rg3 loading were not impaired for the optimum photothermal conversion efficiency of BPs substances.

In addition, our findings reveal that NIR radiation caused more drastic drug release (pH 6.5) than that without NIR, reflected in the increased accumulation of G-Rg3 from BPs/G-Rg3@PLGA. The collective results demonstrated that combination chemotherapy and thermotherapy, along with the precisely calibrated release of drugs, have great benefits when it comes to increasing temperatures.

3.3. BPs@PLGA-manifested preferential localization in primary and metastatic tumors

Breast cancer is a predilection to metastasis to the lungs because of the favorable interaction between cells of the breast cancer and the respective microenvironments of the lung tissue. However, no specific therapeutics have been available to tackle lung metastasis until now, since most therapies are based on primary tumor elimination or degradation to release primary tumor escape from cancer cells. Therefore, we attempted to examine BPs@PLGA lung targetability. To attain this, we have used subline-4T1-luc from 4T1 breast cancer (4T1-luc) cells which, as we have described recently, are highly sensitive to metastatic tendency to the lungs. These NSs have been labeled Cy5.5 in visualizing in vivo BPs@PLGA in order to monitor the fluorescent locations and intensity. The primary organs of the tumors, lung, heart, liver, spleen, and kidney including the fluorescence imaging study had also been obtained at various times during i.v. injections of BP/Cy5.5@PLGA (Figure 3(A)). In these cells, including tumors from 0.5 to 4, 12, and 24 h, a mounting fluorescent signal was detected, and quantified results showed that liver was the primary site of NS accumulations and spleen and kidney, similar to previous studies. In tumors with a remarkable cumulative depositions based upon time-dependent manner (Figure 3(B)), a significant NSs mass was found which suggested the pronounced tumor-dependent tendency of NSs accumulations. The BPs-based nanoagents can be obtained primarily because of the EPR effect for highly effective tumor tissue accumulations. The abnormal vascular framework of tumor tissues allows for nanoparticles to enter the tumor than for other tissue. It is understood that nanoparticles of 10–200 nm have an excellent tendency to the influence of EPR effect on tumors. The EPR effect for treating cancer is used to localize our synthesized BPs nanoagents with a preferred size (∼130 nm) within the tumor.

As 4T1-luc cells had an exotic luciferase reporting gene, a tumor cell could be lighted by i.p. D-luciferin administration and an IVIS System of the Spectrum Imaging bio-luminescence examination. As displayed in Figure 3(C), the fluorescent of BPs/Cy5.5@PLGA in primary tumors was overlapped with luciferase bio-luminescence and indicates an extremely selective target of these NSs on the primary tumors. In particular, as shown in Figure 3(C), we have been investigating luciferase bio-luminescence and BP/Cy5.5@PLGA fluorescence in lung metastatic tumors. The lungs have been shown to overlap these two signals to enhance the robust capacity to penetrate metastatic tumors in the lung (Lee et al., 2018). The above data thereby show that the BPs@PLGA gives a better benefit for combination chemophotothermal (CPT)
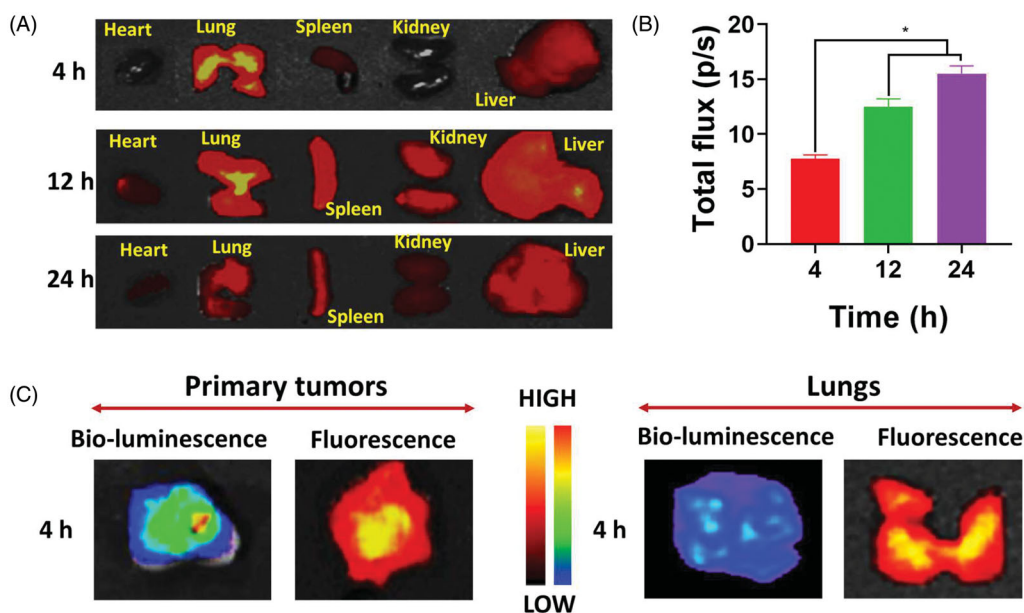

Figure 3. Tissue bio-distributions of BP/G-Rg3@PLGA. (A) Characteristic ex vivo fluorescence image of organs and primary tumors from BPs/G-Rg3@PLGA-treatment mice at injections after various time points. (B) Quantified analysis of fluorescent intensities for the tumor region in the lungs. (C) Mapping of the fluorescent signal and bio-luminescence in lung metastatic tumors and primary tumors at 4 h after injections. The data are represented as the means ± SD; *p< .05.

treatments provided by the hybrid BP/G-Rg3@PLGA, targeting both primary and metastatic tumors. Based on the composite size and structure (a more efficient tumor accumulations structure and size based on current studies), we hypothesis that the PLGA microencapsulation largely contributes to improving our nanodrugs tumor targetability, given its high EPR effects. Both these contain an improved specific target of the metastasis tumors in the lungs along with our BPs@PLGA.

3.4. BPs/G-Rg3@PLGA suppressed lung metastasis in different representations

Xenograft tumors, embedded in the backs of mice/orthotopic designs and focused on primary tumors, are often used in cancer nanomedicine studies, including for metastasis (Cossío et al., 2020). Numerous prior studies, started eradicating primary tumors to prevent metastasis. More suitable tumor models are needed to improve imitate the accurate biological mechanisms and actions of cancer in lung metastasis. Thus, we evaluated BPs@PLGA antimetastasis potency using different designs of mouse-based lung cancer: the orthotopic model and the 4T1-luc injection model developed in previous studies. First, there was the use of the orthotopic models is an excellent models to achieve the efficiency of

chemotherapeutic drug to prevent lung metastasis from the primary tumors of breast cancer. As shown in Figure 4(A), G-Rg3 was not significantly inhibited from primary growth of primary tumors with 10 mg/kg of mice weights, much lesser than that utilized in earlier diagnosis and treatment compared with untreated control. Alternatively, BP/G-Rg3@PLGA, which had the G-Rg3 weight, was about 20% less primary tumor growths without NIR radiations compared to untreated control, as indicated by the tumor growth and the tumor weight (Figures 4(A) and 3(G)). The tumor growth curves reflected the untreated regulation. Combinatory photothermal therapy (PTT) effectively improved, as shown in significantly impaired tumor growth (Figures 4(A) and 3(G)), the efficacy of tumor kills at BP/G-Rg3@PLGA. Three primary tumors, indicating robust CPT potency, have been completely abated in the BPs/G-Rg3@PLGA + NIR group, Figure 4(B). Furthermore, the tumor tissue group of BPs/G-Rg3@PLGA + NIR has been more notably destroyed reflected in the dramatically dying tumor cells and damaged H&E staining (Figure 4(D)).

Many of treatments are restricted by the metastasis of the 4T1-luc lung (Figure 4(F)). In the mice that received G-Rg3 and G-Rg3 + NIR (Figure 4(C), for G-Rg3 + NIR), tumor nodule amounts were shown in the lungs to about 39% and 57%, respectively, in untreated group control. In comparison, the
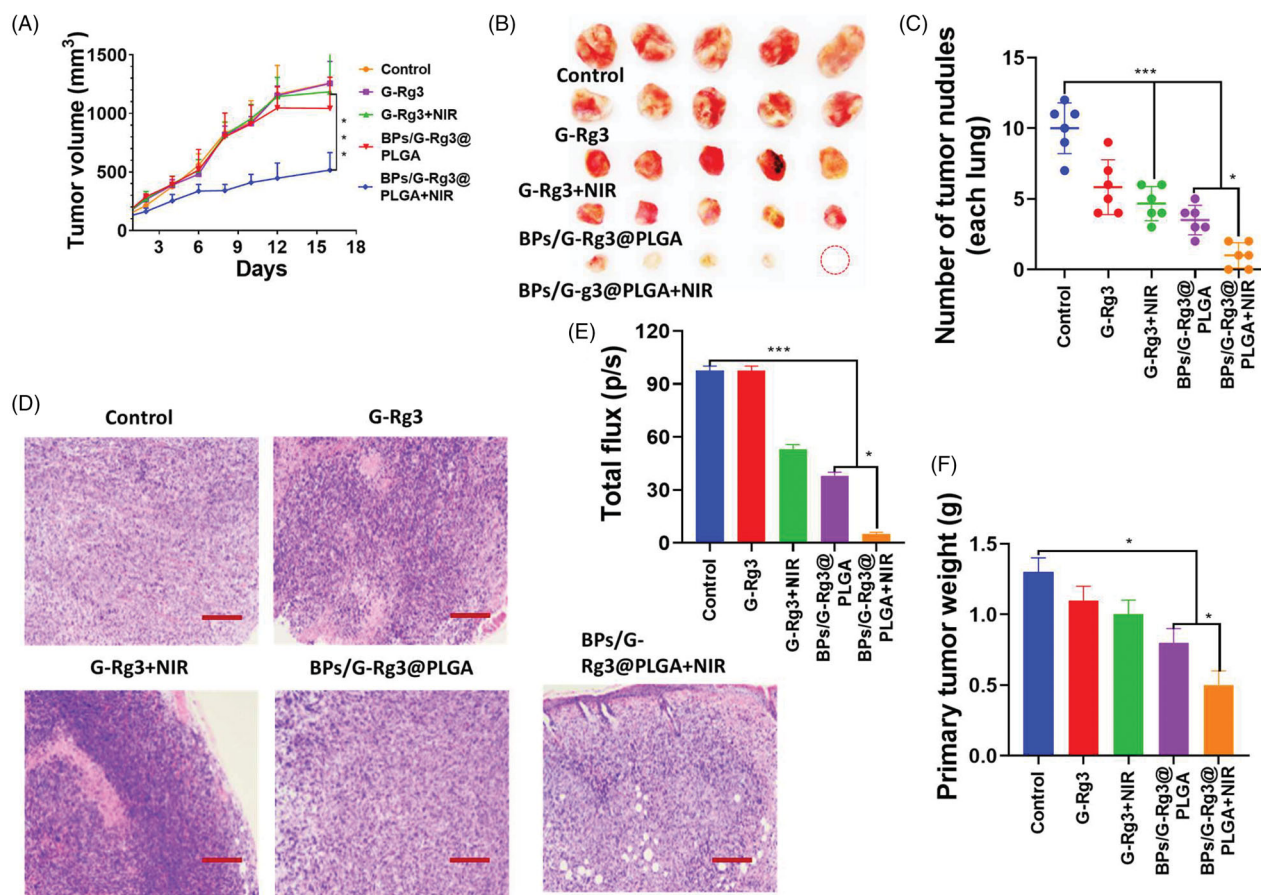

Figure 4. BPs/G-Rg3@PLGA incited lung metastases suppression in the orthotopic animal models. (A) Primary tumor volume growth. (B) Primary tumor photographs after 16 days of growth on the fat mammary pads, where the orthotopic injections of 4T1-luc (1×10^4 cells/per mouse) was achieved, treatment without or with laser NIR radiations followed by G-Rg3 and BPs/G-Rg3@PLGA. (C) Metastatic lung nodules number 16 days after the mice sacrifice, from different groups. (D) H and E staining photographs of tumor pieces from various group displaying the extended pieces. (E) The metastatic lung tumor quantitative data. (F) Primary tumor weights. Scale bar 100 μm. The data are represented as the means ± SD; $*p < .05$, and $***p < .001$.

tumor nodules in mice treatment with BPs/G-Rg3@PLGA with or without the NIR compared to untreated control mice were decreased by 64% and 89%, respectively (Figure 4(C)), while in mice there had been a significant reduction in tumor nodes with BPs/G-Rg3@PLGA + NIR related to BPs/G-Rg3@PLGA without NIR treatment (Figure 4(C)). In the quantification of bio-luminescence similar variations were identified with the largest decrease in the BP/G-Rg3@PLGA + NIR (Figure 4(F)). No bio-luminescent signal was found on sites other than the lungs which highlighted 4T1-luc strong tendency toward the lungs.

Another lung metastasis mouse model was developed, in which four T1-luc cells were injected in the tail vein by mouse, to promote the inhibitory action on metastasis and to eliminate the probability of the inhibitory impact on lung metastasis, caused by the removal of primary tumors (Fang et al., 2018). In G-Rg3, G-Rg3 + NIR and control group over the time period, fast growth in bio-luminescent intensity has been shown, reflecting the fast localizations of 4T1-luc cells for metastasis lung specimens. In BP/G-Rg3@PLGA, approximately 59% and 96% of the rise in bio-luminescence intensity was reduced in comparison to untreated control by the mice without or with NIR (Figure 5(A,B)). Notable factors in the BPs/G-Rg3@PLGA + NIR are the enhancement of the bio-luminescent intensity in mice, and only a small, bio-luminescent signal is eliminated from the BPs/G-Rg3@PLGA + NIR combinatory therapeutic inhibition compared with that of other groups (Figure 5(A,B)). In addition, these major variations have been supported by the direct monitoring of tumor nodule numbers (Figure 5(C)). The survival of such mice has been drastically reduced, particularly in untreated mice, as a result of the successive metastatic tumor formations, apart from the BPs/G-Rg3@PLGA + NIR administration

which has shown considerable survival progress. In addition, the corresponding H&E stain has confirmed the drastic reduction in lung metastatic lesions from mice in comparison with other groups, BPs/G-Rg3@PLGA + NIR administered (Figure 5(D)). Significant cellular havoc occurs in metastatic lung tumors from the BPs/G-Rg3@PLGA + NIR-treated mouse, similar to changes in primary tumors, indicate damaged cells by yellow arrow heads in Figure 5(D) which reveals the considerable toxicities of tumor cells in responses to combined chemothermal therapy.

Unlike tumor tissues, different organs like the kidney, spleen, liver and heart in mice have not received obvious morphological lesions following various administrations, as evidenced by H&E staining methods (Figure 6). In addition, in blood cell counting and biochemical blood samples, no irregular parameters were identified (Figure 7).

These findings show that BP/G-RG 3@PLGA nanocomposites are extremely biocompatible and combination therapeutics are biologically safe. Combining the nanosystems preferential features – outstanding tropism for primary tumors and metastatic tumors and remarkable photothermal results and PTT chemo-toxicity triggers – our results have shown that BPs/G-Rg3@PLGA + NIR therapies have shown excessive potential in limiting breast to lung cancer metastasis.

3.5. BPs/G-Rg3@PLGA induced marked cell death of 4T1-luc cells

We examined *in vitro* the cytotoxic effects of BPs/G-Rg3@PLGA in order to confirm mechanisms for the increased tumor apoptosis in metastatic tumors and primary in responses to BPs/G-Rg3@PLGA + NIR. BPs@PLGA did not
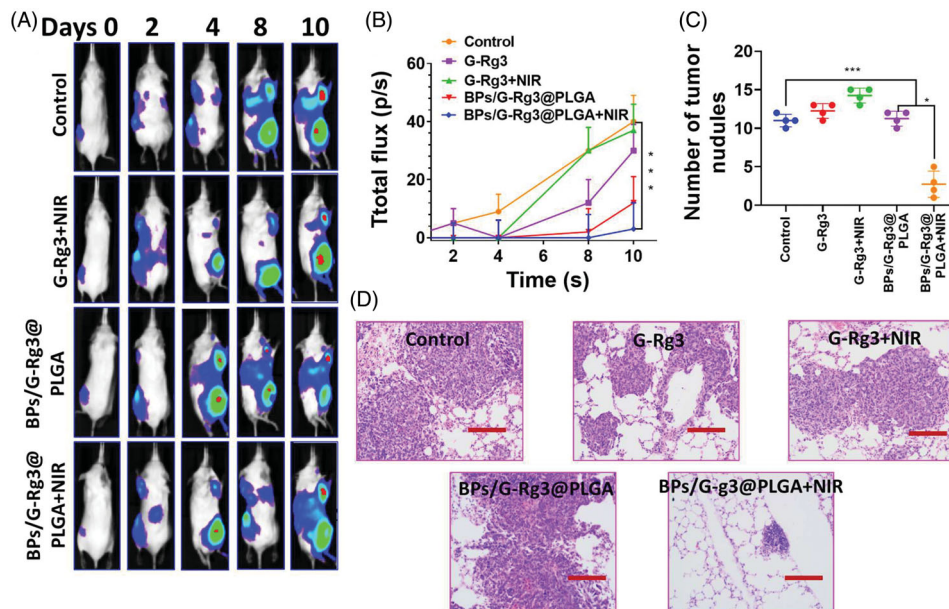

Figure 5. The intratail vein injections model was suppressed by BPs/G-Rg3@PLGA in 4T1-luc cell lung metastasis. (A) After injections of 100 μL of 4T1-luc (15 mg/mL) via the IVIS system of spectrum imaging for whole mice of various group were observed bio-luminescence. (B) Quantified analysis of the bio-luminescent signal in various categories on the lung places in comparisons to untreated control over the time period. (C) At the final stage of the investigation, quantifications of tumor nodules in the lungs of mice. (D) H&E staining photographs in different groups of lung sections. Scale bar 100 μm. The data are represented as the means ± SD; *$p < .05$ and ***$p < .001$.
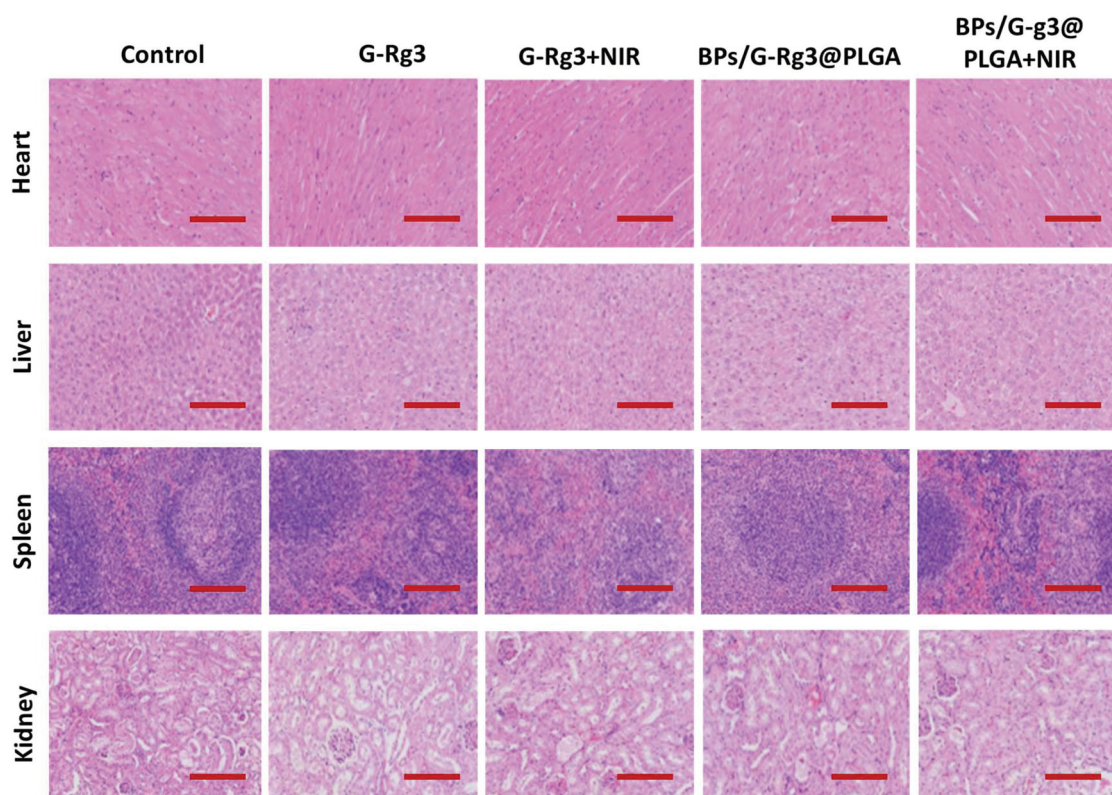
Figure 6. H&E staining of different mice organs after different treatments.
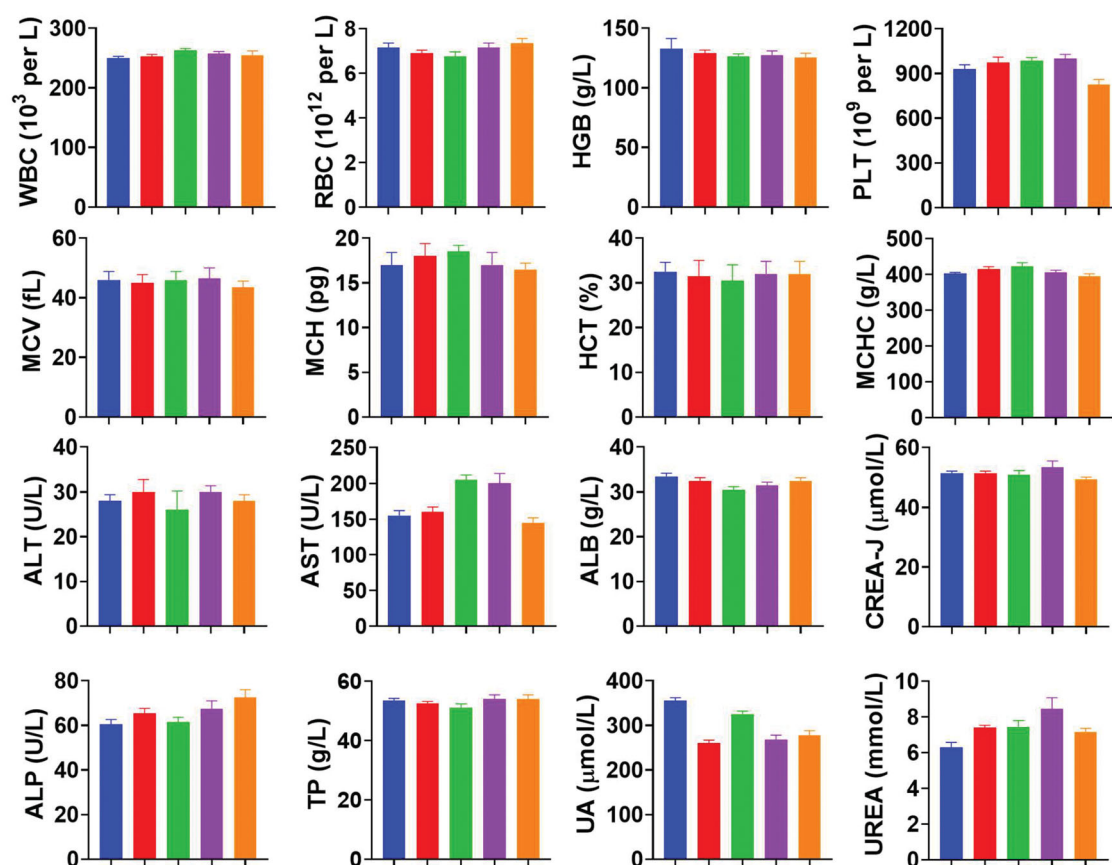

Figure 7. Blood tests and biochemical tests in mice at the end of treatments: control (blue), G-Rg3 (red), G-Rg3 + NIR (green), BPs/G-Rg3@PLGA (purple), BPs/G-Rg3@PLGA + NIR (orange). WBCs: white blood cells; RBCs: red blood cells; HGB: hemoglobin; PLT: platelets; MCV: mean corpuscular volume; MCH: mean corpuscular hemoglobin; HCT: hematocrit; MCHC: mean corpuscular hemoglobin concentration; ALT: alanine aminotransferase; AST: aspartate aminotransferase; ALB: albumin; CREA-J: Creatinine-J; ALP: alkaline phosphatase; TP: total protein; UA: uric acid; CREA: creatinine.
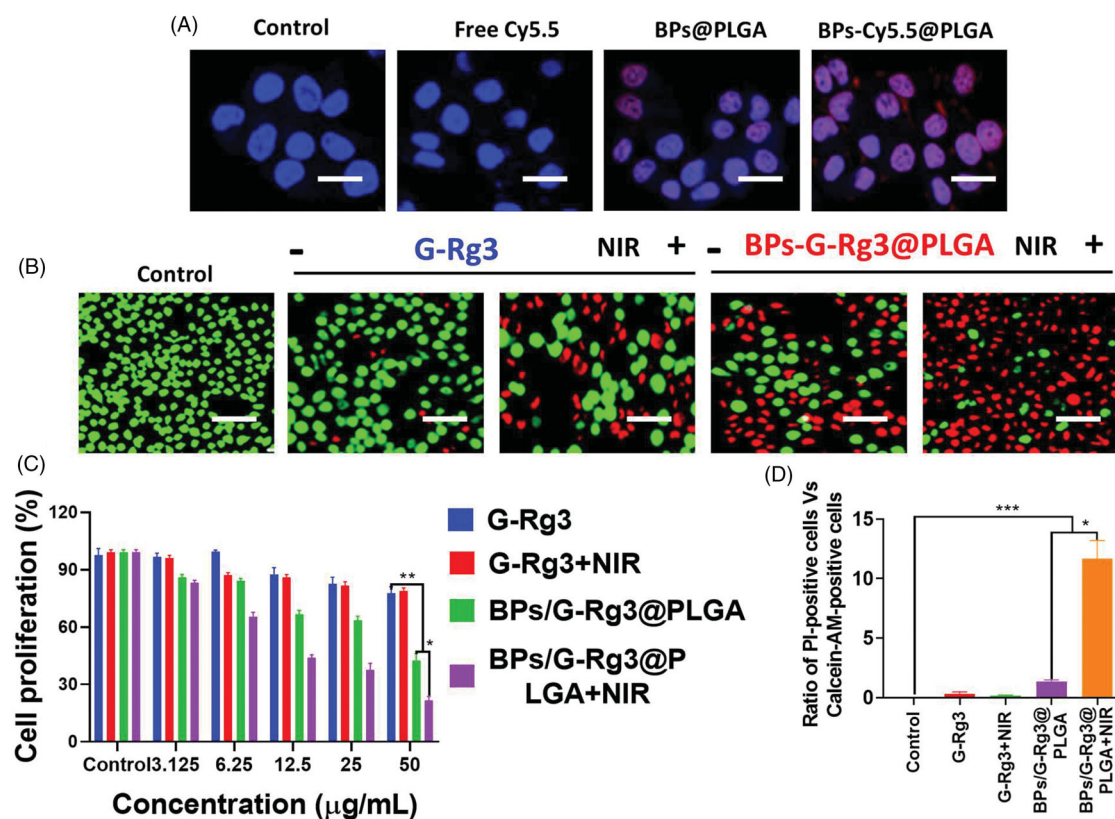
Figure 8. Cellular uptake characterizations and BP/G-Rg3@PLGA-triggered *in vitro* cytotoxicity effects. (A) Fluorescence representation of 4T1-luc cells after incubations with Cy5.5 free label, BPs@PLGA, and Cy5.5-labeled BPs@PLGA at 4 h, as described by laser scanning confocal microscope. (B) Fluorescence representation 4T1-luc cells co-stained with calcein-AM (in green, live cells) and PI (in red, dead cells) after G-Rg3 at 50 µg/mL or BPs/G-Rg3@PLGA at 6 h without or with laser NIR radiations (1.0 W/cm^2, 3 min). (C) Cell proliferation of 4T1-luc cells retorting to various concentration of G-Rg3 or BPs/G-Rg3@PLGA at 24 h without or with laser NIR radiations (1.0 W/cm^2, 3 min), as examined via the CCK-8 analysis. (D) Bar representation shows PI-positive cell ratios and positive calcein-AM cell ratio. The data are represented as the means ± SD; *$p <$ .05, **$p <$ .01, and ***$p <$ .001.

display substantial proliferation in 4T1-luc cells in itself at high concentrations, as the CCK-8 analysis. Subsequently, a CLSM was accomplished to determine the intracellular use of substance in 4T1-luc cells with Cy5.5-labeled BPs@PLGA. Figure 8(A) reveals that, in comparison with no fluorescent in free Cy5.5 sample-treatment cells BPs@PLGA confirms an extreme red fluorescent in the cytoplasm as a suitable delivery drug for nanodrugs. In addition, 4T1-luc cells were treated in a series of similar treatments *in vivo*. As seen in Figure 8(B,C), G-Rg3 has caused slight cell death with or without NIR comparison with untreated cells at a concentration of 50 µg/mL. The concentration of G-Rg3 is much lower than in prior findings, suggesting a low proliferation of G-Rg3 itself toward 4T1-luc cells. It should be noted that this concentration is lesser. However, as seen in approximately 64-fold accumulation for PI-positive cells (Figure 8(B)), and 63% reduction in the cell proliferation (Figure 8(D)), a substantial inhibition in BP/G-Rg3@PLGA-treated 4T1-luc cells was observed for drug delivery platform. Through, in cells that responded in a greater way to BP/G-Rg3@PLGA + NIR, with a higher increase than 100-fold in PI-positive cells and >85% decreased in cell proliferation in accordance with the *in vivo* results mentioned above were more drastic cell growth inhibitions (Figure 8(B,C)). These *in vitro* findings have revealed the multimodal mechanisms induced in proliferation by BPs/G-Rg3@PLGA nanocomposites: the nanocomposite-dependent 'Trojan horse' framework for the delivery of chemotherapy agents, along with combinational CPT toxicity, to cause cell apoptosis.

4. Conclusions

To conclude, we have established a multi-functional nanodrug based on BPs/G-Rg3@PLGA that has a higher tendency to target either primary or lung metastatic tumors effectively and a prominente chemothermal characteristic to control the growth of the tumor in a metastatic direction. BPs/G-Rg3@PLGA reveals that tropism targets both lung metastatic tumors and primary tumors, which are finely tailored to suppress metastatic tumors in the lung through raising the temperatures in laser NIR radiations. Additionally, mechanistic studies interpreted the expedition releases of G-Rg3 from the nanoagents that synergistically causes apoptosis-dependent cell death by heat and thermal therapy. Our nanocomplex also offers remarkable biocompatibility to various organs/tissues. In conjunction with this study, a novel strategies of MTN is introduced for the successful therapy of lung cancer metastases.

Disclosure statement

The authors declare that they have no competing interests.

References

Balaji S, Mohamed Subarkhan MK, Ramesh R, et al. (2020). Synthesis and structure of arene Ru(II) N∧O-chelating complexes: in vitro cytotoxicity and cancer cell death mechanism. Organometallics 39:1366–75.

Biedulska M, Jakóbczyk P, Sosnowska M, et al. (2021). Cytocompatibility of stabilized black phosphorus nanosheets tailored by directly conjugated polymeric micelles for human breast cancer therapy. Sci Rep 11:9304.

Boix-Montesinos P, Soriano-Teruel PM, Armiñán de Benito A, et al. (2021). The past, present, and future of breast cancer models for nanomedicine development. Adv Drug Deliv Rev 173:306–30.

Chen L, Chen C, Chen W, et al. (2018). Biodegradable black phosphorus nanosheets mediate specific delivery of hTERT siRNA for synergistic cancer therapy. ACS Appl Mater Interfaces 10:21137–48.

Cheng G, Zhang Q, Pan J, et al. (2019). Targeting lonidamine to mitochondria mitigates lung tumorigenesis and brain metastasis. Nat Commun 10:2205.

Cossío FP, Esteller M, Berdasco M. (2020). Towards a more precise therapy in cancer: exploring epigenetic complexity. Curr Opin Chem Biol 57:41–9.

Deng B, Tran V, Xie Y, et al. (2017). Efficient electrical control of thin-film black phosphorus bandgap. Nat Commun 8:14474.

Fang T, Lv H, Lv G, et al. (2018). Tumor-derived exosomal miR-1247-3p induces cancer-associated fibroblast activation to foster lung metastasis of liver cancer. Nat Commun 9:191.

Gao R, Li D, Yun Y, Sang N. (2019). Dysfunction of the hippo-yap pathway drives lung cancer metastasis induced by 1-nitropyrene through adhesion molecular activation. Environ Sci Technol Lett 6:270–6.

Geng B, Shen W, Li P, et al. (2019). Carbon dot-passivated black phosphorus nanosheet hybrids for synergistic cancer therapy in the NIR-II window. ACS Appl Mater Interfaces 11:44949–60.

Hu K, Xie L, Zhang Y, et al. (2020). Marriage of black phosphorus and Cu^{2+} as effective photothermal agents for PET-guided combination cancer therapy. Nat Commun 11:2778.

Jiang X, He C, Lin W. (2021). Supramolecular metal-based nanoparticles for drug delivery and cancer therapy. Curr Opin Chem Biol 61:143–53.

Lee W-H, Loo C-Y, Ghadiri M, et al. (2018). The potential to treat lung cancer via inhalation of repurposed drugs. Adv Drug Deliv Rev 133:107–30.

Li Y, Liu Z, Hou Y, et al. (2017). Multifunctional nanoplatform based on black phosphorus quantum dots for bioimaging and photodynamic/photothermal synergistic cancer therapy. ACS Appl Mater Interfaces 9:25098–106.

Li Z, Guo T, Hu Y, et al. (2019). A highly effective π−π stacking strategy to modify black phosphorus with aromatic molecules for cancer theranostics. ACS Appl Mater Interfaces 11:9860–71.

Liang C, Xu L, Song G, Liu Z. (2016). Emerging nanomedicine approaches fighting tumor metastasis: animal models, metastasis-targeted drug delivery, phototherapy, and immunotherapy. Chem Soc Rev 45:6250–69.

Lin C-W, Wang L-K, Wang S-P, et al. (2016). Daxx inhibits hypoxia-induced lung cancer cell metastasis by suppressing the HIF-1α/HDAC1/slug axis. Nat Commun 7:13867.

Low PS, Kularatne SA. (2009). Folate-targeted therapeutic and imaging agents for cancer. Curr Opin Chem Biol 13:256–62.

Mayorga-Martinez CC, Sofer Z, Sedmidubský D, et al. (2018). Metallic impurities in black phosphorus nanoflakes prepared by different synthetic routes. Nanoscale 10:1540–6.

McAllaster JD, Cohen MS. (2011). Role of the lymphatics in cancer metastasis and chemotherapy applications. Adv Drug Deliv Rev 63:867–75.

Mohamed Subarkhan MK, Ramesh R, Liu Y. (2016). Synthesis and molecular structure of arene ruthenium(II) benzhydrazone complexes: impact of substitution at the chelating ligand and arene moiety on antiproliferative activity. New J Chem 40:9813–23.

Mohamed Subarkhan M, Sundar S, Ramesh R. (2018). Synthesis and structure of new binuclear ruthenium(II) arene benzil bis(benzoylhydrazone) complexes: investigation on antiproliferative activity and apoptosis induction. Inorg Chem Front 5:585–96.

Mu X, Wang J-Y, Bai X, et al. (2017). Black phosphorus quantum dot induced oxidative stress and toxicity in living cells and mice. ACS Appl Mater Interfaces 9:20399–409.

Nguyen HT, Byeon JH, Phung CD, et al. (2019). Method for the instant in-flight manufacture of black phosphorus to assemble core@shell nanocomposites for targeted photoimmunotherapy. ACS Appl Mater Interfaces 11:24959–70.

Oku N, Koike C, Tokudome Y, et al. (1997). Application of liposomes for cancer metastasis. Adv Drug Deliv Rev 24:215–23.

Ou W, Byeon JH, Thapa RK, et al. (2018). Plug-and-play nanorization of coarse black phosphorus for targeted chemo-photoimmunotherapy of colorectal cancer. ACS Nano 12:10061–74.

Qian Y, Yuan W-E, Cheng Y, et al. (2019). Concentrically integrative bioassembly of a three-dimensional black phosphorus nanoscaffold for restoring neurogenesis, angiogenesis, and immune homeostasis. Nano Lett 19:8990–9001.

Raucci MG, Fasolino I, Caporali M, et al. (2019). Exfoliated black phosphorus promotes in vitro bone regeneration and suppresses osteosarcoma progression through cancer-related inflammation inhibition. ACS Appl Mater Interfaces 11:9333–42.

Sang W, Zhang Z, Dai Y, Chen X. (2019). Recent advances in nanomaterial-based synergistic combination cancer immunotherapy. Chem Soc Rev 48:3771–810.

Sathiya Kamatchi T, Mohamed Subarkhan MK, Ramesh R, et al. (2020). Investigation into antiproliferative activity and apoptosis mechanism of new arene Ru(II) carbazole-based hydrazone complexes. Dalton Trans 49:11385–95.

Shi S, Zhu X, Zhao Z, et al. (2013). Photothermally enhanced photodynamic therapy based on mesoporous Pd@Ag@mSiO$_2$ nanocarriers. J Mater Chem B 1:1133–41.

Song K-H, Park MS, Nandu TS, et al. (2016). GALNT14 promotes lung-specific breast cancer metastasis by modulating self-renewal and interaction with the lung microenvironment. Nat Commun 7:13796.

Song X, Zhang R, Liang C, et al. (2015). Nano-assemblies of J-aggregates based on a NIR dye as a multifunctional drug carrier for combination cancer therapy. Biomaterials 57:84–92.

Subarkhan MKM, Ramesh R. (2016). Ruthenium(II) arene complexes containing benzhydrazone ligands: synthesis, structure and antiproliferative activity. Inorg Chem Front 3:1245–55.

Suetsugu A, Honma K, Saji S, et al. (2013). Imaging exosome transfer from breast cancer cells to stroma at metastatic sites in orthotopic nude-mouse models. Adv Drug Deliv Rev 65:383–90.

Sung H-J, Ahn J-M, Yoon Y-H, et al. (2011). Identification and validation of SAA as a potential lung cancer biomarker and its involvement in metastatic pathogenesis of lung cancer. J Proteome Res 10:1383–95.

Tian C, Huang Y, Clauser KR, et al. (2021). Suppression of pancreatic ductal adenocarcinoma growth and metastasis by fibrillar collagens produced selectively by tumor cells. Nat Commun 12:2328.

Wan T, Ping Y. (2021). Delivery of genome-editing biomacromolecules for treatment of lung genetic disorders. Adv Drug Deliv Rev 168:196–216.

Wang S, Shao J, Li Z, et al. (2019). Black phosphorus-based multimodal nanoagent: showing targeted combinatory therapeutics against cancer metastasis. Nano Lett 19:5587–94.

Wang S, Zheng H, Zhou L, et al. (2020). Injectable redox and light responsive MnO$_2$ hybrid hydrogel for simultaneous melanoma therapy and multidrug-resistant bacteria-infected wound healing. Biomaterials 260:120314.

Wang Y-T, Tsai C-F, Hong T-C, et al. (2010). An informatics-assisted label-free quantitation strategy that depicts phosphoproteomic profiles in lung cancer cell invasion. J Proteome Res 9: 5582–97.

Wu Z, Lyu Y, Zhang Y, et al. (2021). Large-scale growth of few-layer two-dimensional black phosphorus. Nat Mater 10:1–7.

Xu D, Liu J, Wang Y, et al. (2020). Black phosphorus nanosheet with high thermal conversion efficiency for photodynamic/photothermal/immunotherapy. ACS Biomater Sci Eng 6:4940–8.

Xu Z, Li E, Guo Z, et al. (2016). Design and construction of a multi-organ microfluidic chip mimicking the in vivo microenvironment of lung cancer metastasis. ACS Appl Mater Interfaces 8:25840–7.

Yun Y, Gao R, Yue H, et al. (2017). Sulfate aerosols promote lung cancer metastasis by epigenetically regulating the epithelial-to-mesenchymal transition (EMT). Environ Sci Technol 51:11401–11.

Zhao J, Zhu J, Cao R, et al. (2019). Liquefaction of water on the surface of anisotropic two-dimensional atomic layered black phosphorus. Nat Commun 10:4062.